Analysis and Experimental Validation of an Optimized Gradient-Index Phononic-Crystal Lens

Amir Darabi and Michael J. Leamy*
School of Mechanical Engineering, Georgia Institute of Technology, 771 Ferst Drive NW, Atlanta, Georgia 30332-0405, USA

(Received 3 January 2018; revised manuscript received 5 April 2018; published 29 August 2018)

We propose, analyze, and experimentally verify an optimized gradient-index (GRIN) phononic-crystal lens (PCL) for increased focusing efficiency. The proposed GRIN PCL is formed from a nonsquare lattice of void inclusions in a host plate with transverse variations of the inclusion diameters. With use of a Bloch-based multiple-scattering approach, the refractive index of the lens is made to satisfy a sech profile for flexural waves and then optimized for enhanced harvesting. Under harmonic-plane-wave excitation, the resulting wavefield is analyzed with a ray approximation to characterize the focal points of the lens, followed by representative experiments that demonstrate the validity and effectiveness of the optimized GRIN structure. Furthermore, a piezoelectric energy harvester, located at the first focus of the GRIN PCL, is used to illustrate increases in power gain compared with baseline harvesting.

DOI: 10.1103/PhysRevApplied.10.024045

I. INTRODUCTION

Controlling and directing elastic waves in thin plates has received increased attention in the past few years, driven in part by applications such as flexural lenses [1,2], cloaking devices [3,4], wave-bending structures [5], hyperlenses and enhanced imaging sensors [6], and wave-energy harvesting via piezoelectric transduction [7]. Of primary interest herein is wave-energy harvesting, which aims to convert propagating elastic energy into electrical energy for use in low-powered electronic devices and sensors, for applications such as structural health monitoring and wearable electrical components [8]. In contrast to the vast literature on vibrational-energy harvesting (i.e., standing waves), few studies have considered harvesting of propagating elastic waves. The first studies to appear used Helmholtz resonators [9] for harvesting in-air acoustic waves, and sonic crystals [10] and polarization-patterned piezoelectric solids [11] to harvest elastic waves. Recently, metamaterial-inspired energy-harvesting (MEH) approaches have appeared consisting of periodic arrangements of stubs, inclusions, and voids within a matrix material. The MEH concepts proposed to date have harvested elastic wave energy with use of (i) defect resonators, (ii) funnel-shaped waveguides, (iii) lens-shaped mirrors, or (iv) gradient-index (GRIN) devices [12–16]. Improving on the latter is a primary aim of this work.

GRIN lenses are pass-through devices that focus waves along the propagation axis. The requisite refractive-index gradient has been achieved in phononic devices with use of variations in inclusion diameter and height [17–20], or more recently with use of plate-thickness variations [21]. Lin *et al.* [17] presented the first device based on a GRIN phononic-crystal lens (PCL) by arranging solid cylinders embedded in an epoxy medium into a square two-dimensional lattice. The group velocity (and hence refractive index) transverse to the propagation axis assumes a hyperbolic secant gradient distribution through variations of the cylinder density and elastic moduli. An alternative approach to designing a phononic GRIN device consists in forming an array of inclusions with different radii in the transverse direction. Wu *et al.* [22] demonstrated numerically that the lowest asymmetric Lamb wave in a silicon plate can be focused with an array of void inclusions, which was then further studied both numerically and experimentally by Zhao *et al.* [2]. Other designs then followed, including one by Kurt *et al.* [20] that uses a triangular lattice composed of graded voids in a dielectric host material. A later numerical and experimental study by Wu *et al.* [23] used an AT-cut quartz-plate microlens, and a rectangular-unit-cell study by Zhao *et al.* [24] used constant hole radii in the transverse direction. In all of the aforementioned studies, the GRIN PCLs were configured for high-frequency Lamb waves, which makes the designs unsuitable for use in energy harvesting. To address this concern, Jin *et al.* [18] proposed a flat GRIN device for focusing low-frequency S_0 and A_0 Lamb modes and a circular Luneburg lens by means of simultaneous variations of the inclusions' radii and plate thickness. Most recently, Tol *et al.* [25] presented a GRIN harvesting system incorporating blind holes of differing radii to form a hyperbolic secant refractive index.

*michael.leamy@me.gatech.edu

In all GRIN-PCL studies reviewed with the exception of the study by Zhao *et al.* [24], the lattices have assumed square dimensions, presumably because the quantity being varied is the radius of a cylindrical inclusion. In the case of Zhao *et al.* [24], rectangular unit cells were used with constant transverse radii without formal optimization.

In contrast, this paper proposes a GRIN PCL with nonsquare unit cells to achieve stronger foci and shorter focal lengths, ultimately resulting in smaller devices. The main insight used to configure the lens stems from recognizing the need to increase the refractive-index gradient from unit cell to unit cell, which is accomplished by nonsquare lattices, yielding a larger ratio of inclusion to matrix material. This results in larger bending and tighter foci compared with existing lenses. These ideas are explored with use of a Bloch-based multiple-scattering technique coupled with optimization. Such high-efficiency, high-fidelity modeling of GRIN harvesting concepts is absent in prior GRIN energy-harvesting studies, but is critical for achieving optimized, high-performing refractive-index-gradient distributions. Using a line source to form a plane incident wave, we assess a model of a GRIN-based MEH structure for its ability to focus and harvest wave energy. Finally, an experimental setup is used to verify the model predictions and demonstrate the enhanced harvesting capabilities of the GRIN-PCL design.

II. INTRODUCTION OF THE PROPOSED GRIN PCL

A GRIN lens focuses plane waves by varying its refractive index in the direction transverse to the propagation. Figures 1(a) and 1(b) depict a typical GRIN PCL incorporating holes of transversely differing diameter in an array of equal-sized square unit cells with lattice constant a. In such GRIN structures, the goal is to find an appropriate refractive-index profile that enables strong focusing and collimation. The classic GRIN distribution is characterized by a hyperbolic secant refractive-index profile, which results in minimum aberration [26]. Other functions with the same second-order Taylor-series approximation (i.e., strictly quadratic with zero linear participation) can also be used, but ray theory predicts nonzero aberration. The GRIN proposed herein [Figs. 1(a) and 1(c)] differs from previously studied structures in that it uses nonsquare lattice cells. This straightforward, but important, change is inspired by the need to increase the refractive-index gradient, which in turn results in (i) stronger foci, (ii) shorter focal lengths, and (iii) smaller devices.

III. GRIN-PCL MODELING

The approach taken to model the GRIN PCLs considered relies on multiple subanalysis techniques. First, an appropriate refractive-index profile must be specified, which ultimately determines the location and spread of the GRIN foci. This profile adheres to the refractive-index range achievable by the chosen unit-cell type. Since a discrete lens is considered herein, the profile then specifies a finite number of refractive indices located by each unit cell, which in turn specifies the cell's group velocity, as follows. For small anisotropy, a unit cell's refractive index at a given frequency, ω, can be approximated as [22]

$$n = n_{\Gamma X} = \frac{v_0}{v_{\Gamma X}} = \frac{v_0}{\frac{d\omega}{dk_{\Gamma X}}}, \tag{1}$$

where v_0 is the speed of sound in the host matrix material,

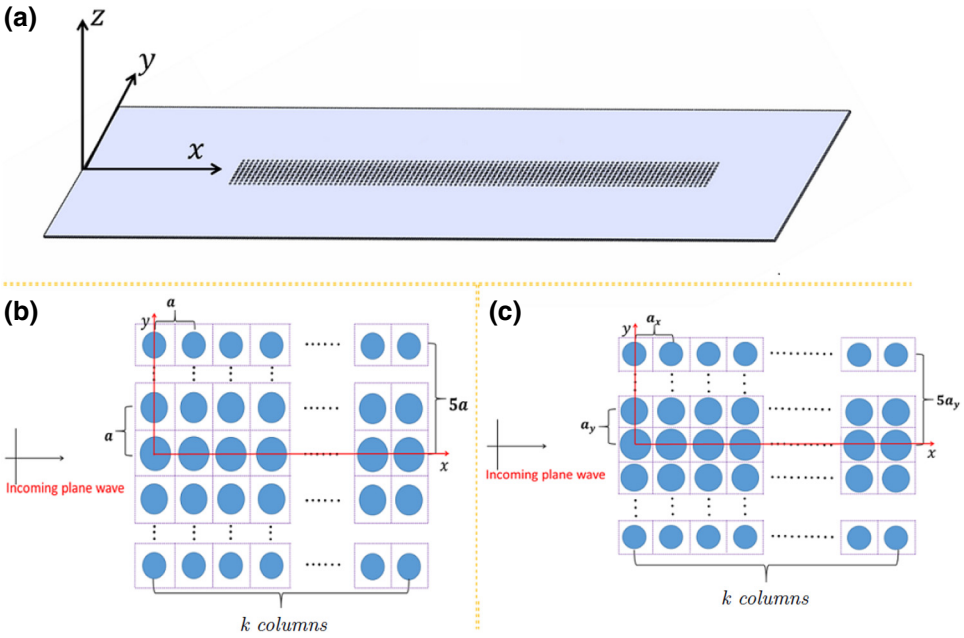

FIG. 1. (a) The GRIN medium with the coordinate axes, (b) previously studied discretized GRIN PCL obtained by varying the inclusions' radii with square unit cells, and (c) proposed discretized GRIN-PCL obtianed by varying the inclusions' radii with nonsquare unit cells.

k the wavenumber, and $v_{\Gamma X}$ the group velocity along the ΓX direction (i.e., wave-propagation direction). A small anisotropy exists in the chosen lattice; for example, at a 45° angle, the matrix material between scatterers is of the largest extent, while for 0° or 90° the extent is the smallest. The rotational symmetry associated with cylindrical inclusions prevents any further anisotropy, and thus the assumption is made that consideration of the group velocity along the ΓX direction is sufficient (this assumption is discussed in Sec. V). In this work, the requisite group velocities are calculated with use of a multiple-scattering technique (described in Sec. III A), and the hole diameter and the unit cell's transverse dimension are varied. After group velocities and refractive indices are determined, a ray-tracing approach (Sec. III B) predicts the locations of the foci and the performance of the as-designed GRIN PCL.

A. Multiple-scattering model

In this section a multiple-scattering approach (see Fig. 2), together with enforcement of a Bloch waveform, is used to calculate the band diagrams, group velocities, and refractive indices associated with each unit cell. The same formulation, without use of Bloch boundary conditions, is used to compute the steady-state response of GRIN-PCL systems. The application of multiple scattering to phononic crystals was introduced in Refs. [27,28]; most recently, multiple scattering was developed for flexural waves [29]. For band diagrams, a single unit cell is assumed to repeat indefinitely in two lattice directions. The scattering coefficients associated with each void are related to a reference unit cell by Bloch's theorem. Truncation of the scattering problem is then performed such that the number of cells N

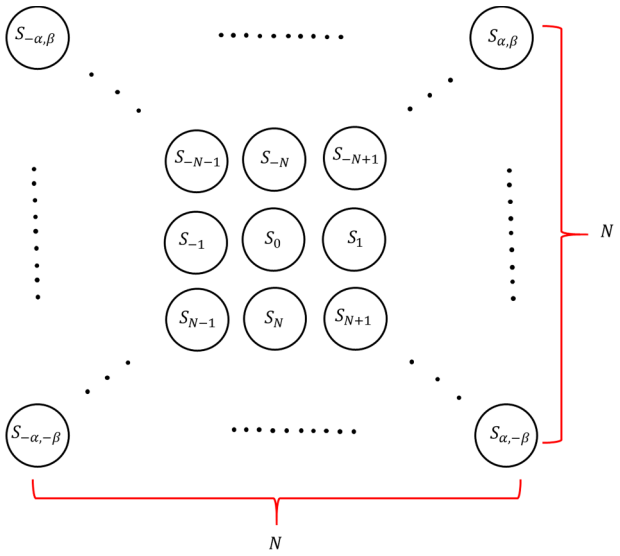

FIG. 2. The multiple-scattering problem to calculate the band structure with use of the Bloch-wave method.

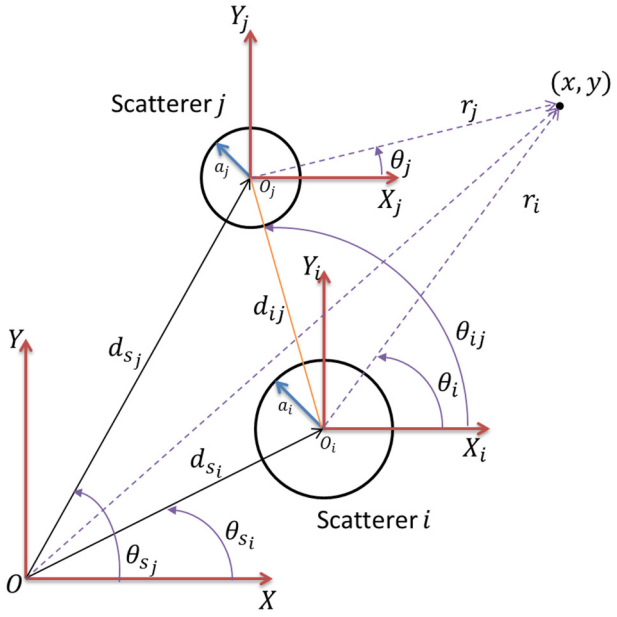

FIG. 3. Geometry for computing the scattered response between two scatterers.

included in each direction is determined by a convergence study.

For the necessary optimization performed herein, multiple-scattering approaches have several advantages over more commonly used numerical approaches (finite element, finite difference, etc.). They do not require discretization of the host medium or need specialized absorbing boundary treatments to mitigate reflections from computational edges. Most importantly, they require many fewer computational degrees of freedom and consume less memory, and thus execute quickly and scale to very large problem sizes. Figure 3 depicts the necessary geometry to compute the incident field from scatterer j scattered by scatterer i. The operating assumption is that an incident wavefield (presumably from a source) and all waves generated by scatterers (except those due to self-scattering) are incident on scatterer i and then subsequently rescattered. This scenario holds for each scatterer j in the system. As shown in Fig. 3, scatterer i with radius a_i is located at (d_{s_i}, θ_{s_i}) with respect to a global-coordinate system. A local-coordinate system (r_i, θ_i), attached to the center (X_i, Y_i) of the ith scatterer, locates any point on the plate. This latter coordinate system is used with a transformation matrix (T matrix) that relates incident- and scattered-wave coefficients for each scatterer. Before application of the T-matrix transformation to each scatterer, all waves must be expressed in the ith scatterer's local-coordinate system. An overview of the method and the formulation of the required T matrix is given next. Full details of the method can be found in Refs. [16,29]

The governing equation for flexural waves in a thin, infinite plate is given as

$$D\nabla^4 w + \rho h \frac{\partial^2 w}{\partial t^2} = f(r,\theta,t), \tag{2}$$

where w denotes the out-of-plane plate displacement, $f(r,\theta,t)$ denotes the distributed external forces, h and ρ denote the thickness and mass density, respectively, and D denotes the plate's flexural stiffness, defined as $Eh^3/12(1-\nu^2)$, where E represents Young's modulus and ν represents Poission's ratio. All incident and scattered waves considered herein satisfy Eq. (2). The incident wavefield in the plate is represented in Bessel form as

$$w^{\text{inc}} = [\{\mathbf{A}^p\}^T\{\mathbf{J}(r,\theta)\} + \{\mathbf{A}^e\}^T\{\mathbf{I}(r,\theta)\}]e^{\hat{i}\omega t}, \tag{3}$$

and the wavefield scattered by the jth individual cylindrical scatterer with radius a_j is represented as

$$w_j^{\text{scr}} = (\{\mathbf{B}_j^p\}^T\{\mathbf{H}(r_j,\theta_j)\} + \{\mathbf{B}_j^e\}^T\{\mathbf{K}(r_j,\theta_j)\})e^{\hat{i}\omega t}, \tag{4}$$

where for any $\mathbf{\Omega}$, $\{\mathbf{\Omega}(r,\theta)\}_n = \Omega_n(k_B r)e^{\hat{i}n\theta}$, n denotes the order of the Bessel function and k_B denotes the flexural wave number related to excitation frequency ω by $k_B^2 = \omega\sqrt{\rho h/D}$. $\{\mathbf{A}^p\}$ and $\{\mathbf{A}^e\}$ denote arrays containing the expansion (or wave) coefficients of the propagating and and evanescent incident waves, respectively; see Ref. [29] for full expressions for plane waves and point sources. Similarly, $\{\mathbf{B}_j^p\}$ and $\{\mathbf{B}_j^e\}$ hold expansion (or wave) coefficients for propagating and evanescent scattered waves, respectively. In addition, $\{\mathbf{J}(r,\theta)\}$, $\{\mathbf{I}(r,\theta)\}$, $\{\mathbf{H}(r,\theta)\}$, and $\{\mathbf{K}(r,\theta)\}$ denote arrays holding Bessel functions of the first kind, modified Bessel functions of the first kind, Hankel functions of the first kind, and modified Bessel functions of the second kind, respectively. Bessel functions $\mathbf{J}(r,\theta)$ and $\mathbf{I}(r,\theta)$ represent incident waves due to their finite value at the origin, while $\mathbf{H}(r,\theta)$ and $\mathbf{K}(r,\theta)$ represent scattered waves due to their boundedness at infinity.

If we express the incident and all scattered waves in the ith scatterer's coordinate system, the scatterer's T matrix ($[\boldsymbol{\tau}_i]$) yields an expression relating the wave coefficients at i to those at all other scatterers $j \neq i, j \in \{1,2,\ldots,z\}$:

$$\{\mathbf{B}_i\} = [\boldsymbol{\tau}_i]\left(\{\mathbf{A}_i\} + \sum_{j=1,j\neq i}^{z} [\mathscr{R}_{ji}]^T\{\mathbf{B}_j\}\right), \tag{5}$$

where z is the number of scatterers in the multiple-scattering problem and

$$\mathscr{R}_{ji} = \begin{bmatrix} [\mathbf{R}_{ji}^p] & 0 \\ 0 & [\mathbf{R}_{ji}^e] \end{bmatrix} \tag{6}$$

transforms wave coefficients from the jth scatterer's local-coordinate system to the ith scatterer's local-coordinate system with elements

$$[R_{ij}^p]_{nm} = e^{\hat{i}(n-m)\theta_{ij}} H_{n-m}(k_B d_{ij}), \tag{7}$$

$$[R_{ij}^e]_{nm} = (-1)^m e^{\hat{i}(n-m)\theta_{ij}} K_{n-m}(k_B d_{ij}). \tag{8}$$

In all cases, $\{\mathbf{A}_k\} = \{\begin{smallmatrix}\{\mathbf{A}_k^p\}\\ \{\mathbf{A}_k^e\}\end{smallmatrix}\}$ and $\{\mathbf{B}_k\} = \{\begin{smallmatrix}\{\mathbf{B}_k^p\}\\ \{\mathbf{B}_k^e\}\end{smallmatrix}\}$ denote the generalized expansion coefficients in the kth scatterer's local-coordinate system. Collecting all z instances of Eq. (5) results in the following relationship for the unknown coefficients of the scattered waves:

$$\{\mathscr{B}\} = [\mathscr{L}]\{\mathscr{A}\}, \tag{9}$$

where

$$\{\mathscr{B}\} = \begin{Bmatrix} \{\mathbf{B}_1\} \\ \{\mathbf{B}_2\} \\ \cdot \\ \cdot \\ \cdot \\ \{\mathbf{B}_Z\} \end{Bmatrix}, \quad \{\mathscr{A}\} = \begin{Bmatrix} [\boldsymbol{\tau}_1]\{\mathbf{A}_1\} \\ [\boldsymbol{\tau}_2]\{\mathbf{A}_2\} \\ \cdot \\ \cdot \\ \cdot \\ [\boldsymbol{\tau}_Z]\{\mathbf{A}_Z\} \end{Bmatrix}, \tag{10}$$

and the elements of $[\mathscr{L}]$ hold transformation matrices. To compute the steady-state response of the field, a plane-wave source located at x_s from the first column of scatterers is used to generate an incident wavefield. Similarly to what was done in Ref. [29], the incident plane wave is modeled for each single scatterer as per Eq. (3), and a Hankel transformation is applied to find the incident-wave coefficients:

$$\{A_i^p\}_n = e^{\hat{i}k_B X_i}\hat{i}^n, \tag{11}$$

$$\{A_i^e\}_n = 0, \tag{12}$$

where X_i is the distance between the location of the plane-wave source and the ith scatterer.

Next, the multiple-scattering approach is specialized for computing dispersion and group velocities using Bloch's theorem. First, the incident-wave coefficients are removed from Eq. (5) and the system is reduced to an $N \times N$ array of scatterers:

$$\{\mathbf{B}_i\} = [\boldsymbol{\tau}_i]\sum_{j=1,j\neq i}^{N^2} [\mathscr{R}_{ji}]^T\{\mathbf{B}_j\}. \tag{13}$$

Then, a Bloch solution is sought of the form $\{\mathbf{B}_j\}(\omega) = \{\mathbf{B}_0\}(\omega)e^{\hat{i}\lambda_j\mu_x}e^{\hat{i}\gamma_j\mu_y}$ such that

$$\{\mathbf{B}_0\} = \sum_{j=1,j\neq i}^{N^2} [\boldsymbol{\tau}_j][\mathscr{R}_{j0}]^T\{\mathbf{B}_0\}e^{\hat{i}\lambda\mu_x}e^{\hat{i}\gamma\mu_y}, \tag{14}$$

where $\boldsymbol{\mu} = \mu_x \boldsymbol{e_x} + \mu_y \boldsymbol{e_y}$ is the dimensionless wavevector such that $\mu_x \equiv k_x a_x$ and $\mu_y \equiv k_y a_y$; λ and γ denote integers locating the j th unit cell away from the reference unit cell S_0; and k_x and k_y are the wavenumbers in the x direction and the y direction, respectively. Note that $\lambda = \gamma = 0$ for the reference unit cell (S_0). For this substudy, the wave propagates in the x direction such that $k_x = k_B$ and $k_y = 0$. Placing all the coefficients $\{\boldsymbol{B_0}\}$ on one side results in the following relationship for the unknown coefficients of the scattered wave:

$$[\mathscr{L}_0(k_B, \omega)]\{\boldsymbol{B_0}\} = \vec{0}, \tag{15}$$

where the elements of $\mathscr{L}_0$ contain k_B and the T and transformation matrices. Setting the determinant of the $\mathscr{L}_0$ matrix to zero yields the desired dispersion relationship relating $k_{\Gamma X}$ (i.e., k_B) to ω. This is done numerically due to the complexity of matrix $\mathscr{L}_0$ by specifying k_B and then finding the frequencies ω yielding the determinant zeroes. Finally, with use of Eq. (1), the refractive index of the corresponding unit cell can be calculated. A convergence study of the band structure is performed by inclusion of successive levels of neighboring scatterers (nearest neighbors, next-nearest neighbors, etc.), together with the Bloch theorem. This can be observed from Eq. (13), where λ and γ locate scatterers away from the reference unit cell, in the x direction and the y direction, respectively, and a Bloch form of the solution has been invoked. The number of scatterers included is truncated in each direction when the band structure converges to within 5% for any frequency.

For the Bloch-wave multiple-scattering technique described above, Fig. 4 depicts the band structure calculated for an example unit cell. The band structure is computed by our sweeping the dimensionless wavenumber from 0 to π along the propagation direction (i.e., ΓX) for the case of an aluminum plate (thickness 3.175 mm).

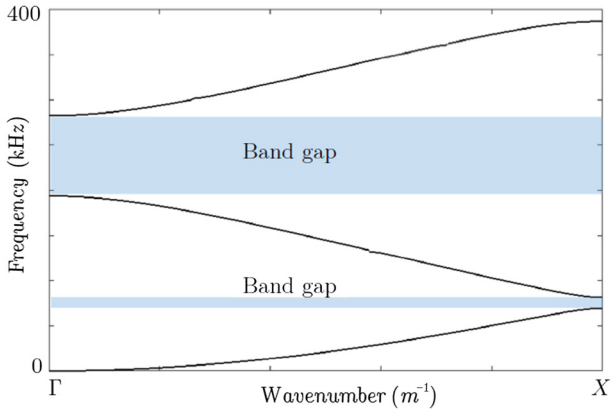

FIG. 4. Computed band structure for an example unit cell. All wavenumbers correspond to waves propagating in the ΓX direction.

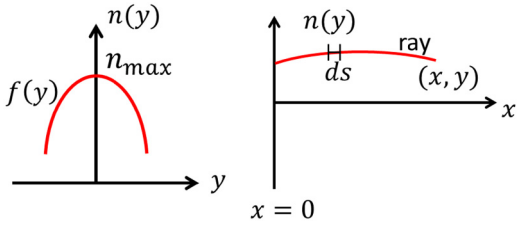

FIG. 5. (a) Refractive-index profile and (b) ray propagation in a GRIN medium with a desired profile.

The example nonsquare unit cell contains a centered hole (diameter 4 mm) and has size of $8 \times 6\,\mathrm{mm}^2$. Since only transverse plate motions are modeled, all branches belong to the first-asymmetric-mode type (i.e., A_0 Lamb waves). The presence of the void, together with repetition of the unit cell, leads to a Bragg-scattering band gap. This band gap limits the working range of the GRIN PCL since frequencies in the band gap result in purely reflected waves.

B. Ray-tracing analysis

The refractive-index profile of a two-dimensional GRIN medium along the transverse direction (y-axis) is defined as [26]

$$n(y) = n_{\max} f(y), \tag{16}$$

where $n_{\max}$ is the refractive index along the center of the axis of the medium (x-axis) and f is a function with a convex shape with maximum value at $y = 0$ [see Fig. 5(a)].

The ray equation [30] for the wave propagating through the designed waveguide is obtained from the expression of a differential arc length along a ray joining any two points of the medium, as shown in Fig. 5(b):

$$\frac{d}{ds}\left[n(\mathbf{r})\frac{d\mathbf{r}}{ds}\right] = \nabla n(\mathbf{r}), \tag{17}$$

where $\mathbf{r}(s) = x(s)\hat{i} + y(s)\hat{j}$ denotes the position vector and $ds = \sqrt{dx(s)^2 + dy(s)^2}$ denotes the arc length. The appropriate boundary conditions for an incoming plane wave are $x(0) = 0$, $dx/ds(0) = 1$, $y(0) = C$, and $dy/ds(0) = 0$. In the present application the refractive index is solely a function of y (i.e., $dn/dx = 0$). Equation (17) is then solved numerically (e.g., with use of a finite-difference method) for several choices of C, where each C prescribes a single ray.

IV. GRIN-PCL OPTIMIZATION

The described modeling approaches, together with optimization, are used to configure a nonsquare GRIN PCL with increased focusing efficiency. The GRIN structure uses through holes (i.e., scatterers) of differing diameter

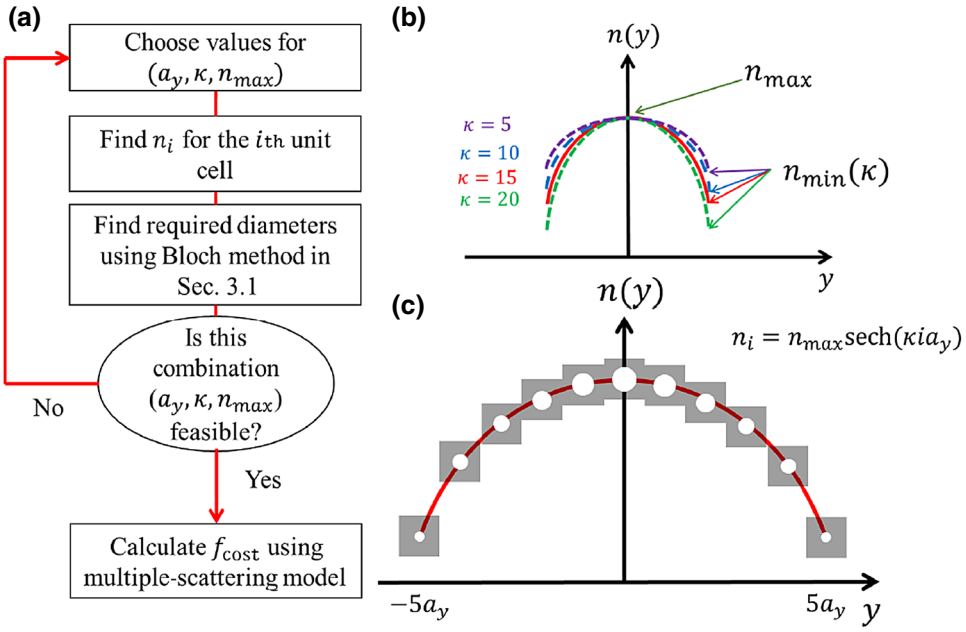

FIG. 6. (a) Step-by-step algorithm describing the optimization process for the proposed GRIN PCL, (b) qualitative comparison of the different refractive index ratios (n_{max}/n_{min}), and (c) distribution and size of the unit cells in the GRIN medium.

constrained to a column of 11 holes evenly spaced in the y direction (located at $Y_i = 0, \pm a_y, \pm 2a_y, \pm 3a_y, \pm 4a_y, \pm 5a_y$ mm) and repeated every a_x mm in the x direction. The hole diameters are adjusted to achieve an appropriate refractive-index profile of the form $n(y) = n_{max}\mathrm{sech}(\kappa y)$, where n_{max} and κ represent optimization parameters. The third optimization parameter is the y direction lattice constant, a_y. As depicted in Fig. 6(a), these three parameters drive an ad hoc optimization procedure in which each candidate set generates a refractive-index profile [see Fig. 6(b)] where for fixed a_y and n_{max} increasing κ both increases the curvature of the profile and decreases the minimum index of refraction n_{min}. Following specification of the three optimization parameters, the profile is discretized [see Fig. 6(c)] with use of a_y as the discretization size to locate the requisite refractive indices, $n_i = n_{max}\mathrm{sech}(\kappa i a_y)$, $i = 0, 1, 2, \ldots, 5$. Finally, the diameters necessary to achieve these refractive indices are found with use of the Bloch-wave multiple-scattering technique. For some choices of a_y, κ, and n_{max}, the diameters needed to achieve the requisite refractive indices cannot be found, and thus this set is determined to be infeasible. Any feasible combination is assigned a cost f_{cost}, described in more detail below, and computed in part by steady-state multiple-scattering calculations. The optimized GRIN PCL is the one for which this cost is driven close to a minimum.

For a GRIN PCL with a large refractive-index ratio (i.e., $n_{max}/n_{min} \gg 1$), the related focal spots are closer to the lens, while for a smaller ratio, the foci are further from the source of the incident wave. Figure 7 depicts ray paths in a continuous-profile GRIN PCL for different refractive-index ratios. As illustrated, for a GRIN PCL with foci closer to the source (implying smaller device size), the ratio of the refractive index at the center axis and edges should be larger. Conversely, when the maximum refractive index is large compared with the host-layer refractive index, more energy is reflected from the GRIN PCL due to the discrete nature of the refractive-index profile, resulting in less focused energy. Consequently, a clear trade-off exists when one is choosing a discrete refractive-index profile, motivating the use of a weighted cost function. Herein, the cost of any candidate profile is divided into three considerations. The first is the average focal power P_{focal} (computed by multiplication of the averaged steady-state velocity of sampled points in the focal spot by the area of the focal spot), the second is the focal spacing l_{focal} (computed by ray tracing and confirmed by steady-state multiple-scattering calculations), and the third is the operating band of the GRIN f_{max} (determined from the Bloch-wave multiple scattering and the predicted band-gap lower frequency). This leads to the weighted cost function

$$f_{cost} = -w_1 P_{focal} + w_2 l_{focal} - w_3 f_{max}, \qquad (18)$$

where w_1, w_2, and w_3 denote weights.

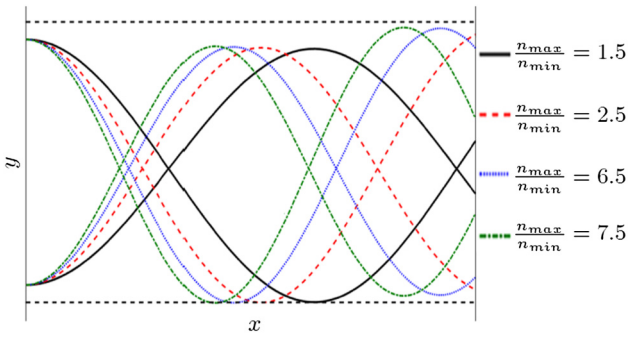

FIG. 7. Ray-path trajectories for the wave propagating in a GRIN medium with different refractive-index-ratio profiles.

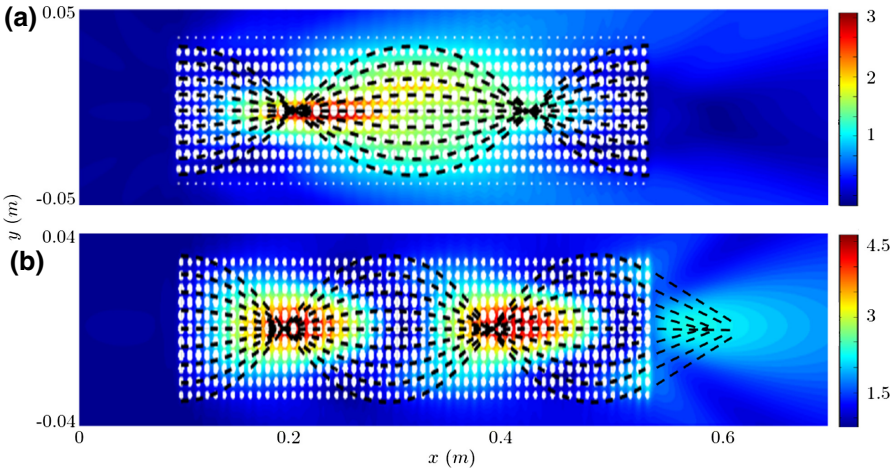

FIG. 8. Multiple-scattering predictions of the normalized wavefield displacement for (a) the GRIN PCL inspired by Tol *et al.* and (b) optimized, nonsquare GRIN-PCL. Dashed lines represent ray-path trajectories.

The GRIN PCL considered by Tol *et al.* [25] is chosen to highlight the proposed analysis procedures and optimization approach. Their system represents the first experimentally verified GRIN PCL used for the purposes of harvesting wave energy. The goal herein is to use the presented analysis tools and ad hoc optimization procedure to improve the harvesting performance and decrease the size of the GRIN-PCL system of Tol *et al.*

Tol *et al.* considered square lattice cells ($a_x = a_y = 8$ mm) with blind-hole diameters of 7.00, 6.93, 6.63, 5.99, 4.81, and 2.00 mm in an aluminum plate of thickness 3.175 mm to obtain a hyperbolic refractive-index distribution, $n = 1.186\ \mathrm{sech}(14.5y)$. Rather than blind holes, we consider through holes; this difference, however, has little effect on the analysis procedures and optimization conclusions since it amounts to only a small change in the T-matrix scattering efficiency. Figure 8(a) depicts the predicted steady-state wavefield response of the GRIN PCL inspired by Tol *et al.* generated with multiple scattering at 50 kHz. Also shown are the corresponding ray-path trajectories. Note that displacement amplitudes are normalized with respect to the source displacement. As shown, the incident plane wave is gradually bent toward the center axis, where the refractive index is the highest (or the wave speed is the lowest), resulting in convergence at a focal spot. The maximum amplitude of the wave appears at $x \approx 21$ cm, or $x_f \approx 11$ cm from the left edge of the GRIN PCL. Ray tracing predicts this distance to be $x_f = 10.8$ cm.

The optimization procedure is applied next to increase the focal power while decreasing the device size. The optimization weights are chosen as $w_1 = 400, w_2 = 30$, and $w_3 = 2/1000$. Since the most important parameter for designing a GRIN PCL for energy-harvesting purposes is the power of the foci, this parameter is chosen to have the largest weight. The second-most-important parameter is the length of the focal point, whereby shorter focal lengths are more desirable. Finally, the operating band is chosen to have the least weight. All weights are chosen after some calculations to ensure one weight will not dominate all others during the optimization process. Eight different values (from 4 to 8 mm in 0.5-mm increments) are chosen for a_y, with a_x remaining at 8 mm. Then, for a fixed a_y, the refractive-index-profile parameters (i.e., $n_{\max}$ and κ) are varied to optimize the refractive-index profile. The maximum refractive index $n_{\max}$ is varied from 1.1 to 2.5 in increments of 0.1, while κ is varied from 10 to 24 in increments of 0.1. The parameter ranges for a_y, $n_{\max}$, and κ are those obtained for the system of Tol *et al.*

Following optimization at 50 kHz, the final GRIN PCL is characterized by a lattice spacing of $a_y = 5.5$ mm and

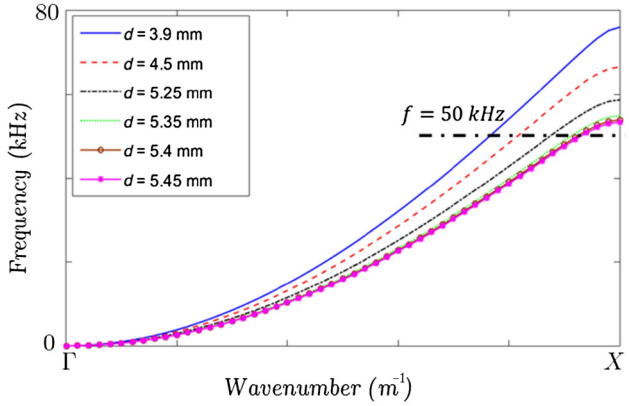

Location	Diameter (mm)	Refractive index
0	5.45	2.15
a_y	5.4	2.13
$2a_y$	5.35	2.10
$3a_y$	5.25	2.04
$4a_y$	4.5	1.97
$5a_y$	3.9	1.88

FIG. 9. Unit-cell dispersion curves for the optimized GRIN PCL with $a_x = 8$ mm and $a_y = 5.5$ mm (top), and locations, through -ole diameters, and resulting refractive indices computed at 50 kHz (bottom).

refractive-index profile $n = 2.15\ \mathrm{sech}(19y)$. The device contains through holes with diameters $d = 5.45$, 5.4, 5.35, 5.2, 4.5, and 3.90 mm, corresponding to refractive indices of $n = 2.15$, 2.13, 2.10, 2.04, 1.97, and 1.88. Figure 9 shows the dispersion curves of the final lens for each of the different unit cells. As shown, by increase of the filling factor (area of the hole to the area of the lattice), $v_{\Gamma X}$ becomes smaller, resulting in a larger refractive index for the corresponding hole [see Eq. (1)]. Accordingly, for smaller through holes (i.e., smaller refractive index), an incident plane wave travels faster in comparison with that in unit cells with larger through holes.

Figure 8(b) presents the multiple-scattering-predicted steady-state scattered displacement wavefield for the optimized GRIN PCL at 50 kHz. Compared with the lens inspired by Tol *et al.*, the optimized lens results in a shorter focal length due to the larger refractive-index ratio $n_{\max}/n_{\min}$. The predicted focal distance is $x_F \approx 9$ cm, which compares well with the ray-path-predicted value of $x_F = 8.5$ cm, and is 2 cm shorter than that of the unoptimized lens for a plane incoming wave. In addition, at the first focal point, the proposed design produces a higher displacement concentrated over a smaller area. Moreover, the second focal point is significantly more pronounced (i.e., less aberration) than in the unoptimized case. Finally, because of the decreased device size, a third focal point begins to emerge, and continues past the right edge of the GRIN PCL.

V. EXPERIMENTAL APPARATUS AND VALIDATION

A set of experiments are performed to demonstrate the performance of the optimized GRIN PCL. Figure 10 details the experimental setup. A Polytec PSV-400 scanning laser Doppler vibrometer measures the out-of-plane surface velocity field, while an oscilloscope measures the harvester voltage. The GRIN PCL is formed with an aluminum plate of thickness $h_s = 3.175$ mm. The scattered-wavefield displacement is scanned over a $70 \times 10\,\mathrm{cm}^2$ area, with use of the back side of the plate, with a 250×250 grid resolution. Six epoxy-bonded piezoelectric transducers (Steiner Martins SMPL30W30T1121, 3M DP270 epoxy adhesive) with thickness $h_p = 0.2$ mm, located 10 cm from the first unit cell, excite the system in response to a generated 200-mV (peak-to-peak) voltage profile by five cycles of a sinusoidal wave, with use of a function generator (Agilent 33220A) coupled to a voltage amplifier (B&K 1040L). Each rectangular piezoelectric transducer measures $7 \times 7\ \mathrm{mm}^2$ and has an effective capacitance of $C_p = 1.5$ nF. The setup uses two circular harvesting transducers (Steiner Martins SMD03T04S311) with a radius of 1.5 mm and an effective capacitance of $C_p = 3$ nF. These piezoelectric transducers are smaller than the size of the focal area. All scatterers in the host plate have a depth of 3 mm (not 3.175 mm), which is used instead of through holes to facilitate measurement with the scanning vibrometer. Absorbing pitch tape is used on the plate's perimeter to prevent reflection of waves from boundaries. Proper triggering of the laser measurements allows the reconstruction of the out-of-plane velocity field, while time integration of the recorded responses yields rms distributions.

Figure 11 displays the scattered wavefields obtained experimentally for four operating frequencies chosen to demonstrate the onset and loss of focusing, and clearly demonstrates the existence of two foci along the centerline of the aluminum plate. The measured wavefields in Fig. 11 resemble closely those predicted by multiple scattering. Specifically, at the designed-for operating frequency of 50

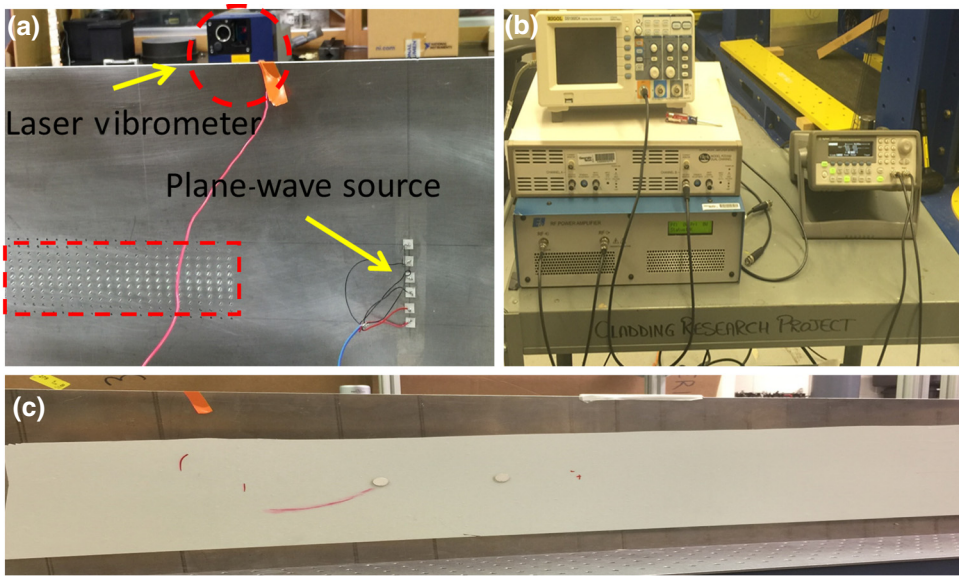

FIG. 10. Experimental setup: (a) aluminum plate hosting piezoelectric transducers to excite waves and laser vibrometer used to measure the back-side transverse plate velocity, (b) function generator and amplifier for generating the requisite voltage, and (c) overall setup showing the mounted plate and reflective material on the back side.

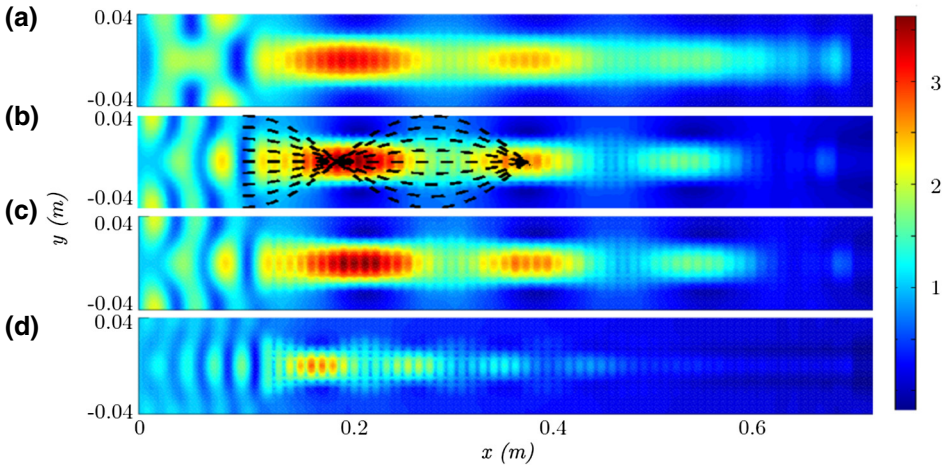

FIG. 11. Experimentally measured normalized wavefield displacement for (a) $f = 40$ kHz, (b) $f = 50$ kHz, (c) $f = 60$ kHz, and (d) $f = 70$ kHz. In (b), the dashed black line shows the theoretical ray path [see also Fig. 8(b)].

kHz, the first focal point occurs at approximately 10 cm from the leading edge of the GRIN PCL, and the second occurs at 27 cm; this compares well with the multiple-scattering predictions of 9 and 28.5 cm, respectively. Weak leakage of wave energy is observed close to the foci due to the imperfect depth of the holes. As expected, the most-focused case is at the designed-for operating frequency, where the frequency-dependent refractive-index profile follows the sech shape. Here, the ratio of the maximum displacement to the minimum displacement (the amplitude of the plane wave) is close to 3 (see Fig. 11). For an excitation frequency of $f = 40$ kHz, the two foci occupy a larger area due to longer wavelengths; conversely these areas are smaller for $f = 70$ kHz due to a smaller wavelength. On the basis of the band structure of the lens (Fig. 9), for frequencies higher than $f = 60$ kHz, some of the unit cells become inactive (i.e., the frequency is above the cutoff frequency and pure reflection results). In summary, the optimized GRIN PCL operates over a 20-kHz band starting at 40 kHz, resulting in broadband performance. Anisotropy in the refractive index, at a frequency of 50 kHz, is small as evidenced by the good agreement between experimental and theoretical results.

Next, the harvesting potential of the optimized GRIN PCL is assessed. A resistance substituter (IET Labs model RS-200) is attached to the piezoelectric harvesters and used to generate resistances from 10 Ω (close to short-circuit condition) to 100 kΩ (close to open-circuit condition). The first harvester is located 10 cm from the leading edge (i.e., the first focal point), and the second baseline harvester is located 20 cm from the leading edge (i.e., where the plane wave is again reconstituted). With use of an oscilloscope, the voltage across the resistor is measured, and the average output power is calculated accordingly. Figure 12 compares the experimentally measured peak voltage of the harvesters at the first focal point and the baseline for different values of load resistance. The piezoelectric voltage at the focal point is greater than the baseline voltage for all values of load resistance. Similarly, Fig. 13 documents the experimentally measured average power output generated by the piezoelectric disks versus load resistance. The generated power obtained with the focal harvester is 2 orders of magnitude greater than the baseline power. The optimized output power represents an increase of approximately 12-fold compared with the case with a near-open-circuit condition. Moreover, the peak resistance of the power plot roughly conforms to that

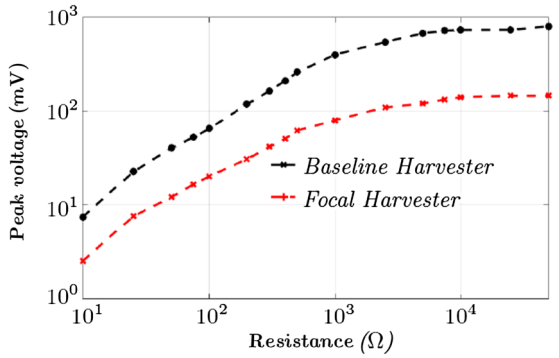

FIG. 12. Experimentally measured peak voltage for various values of load resistance.

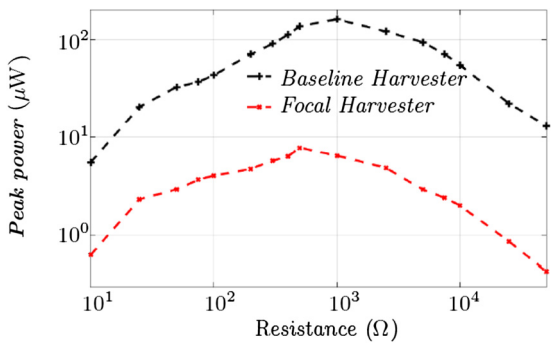

FIG. 13. Experimentally measured average power for various values of load resistance.

predicted with use of a classical weakly coupled prediction of $(1/\omega Cp) = 1000$.

VI. CONCLUSIONS

We present an optimized GRIN PCL and harvester system using nonsquare unit cells. To support its analysis and optimization, high-fidelity multiple scattering, ray tracing, and an ad hoc optimization procedure are also detailed. Starting from a previous GRIN PCL, we perform the analysis and optimization procedures to significantly increase the focal power while decreasing the device size. Experiments verify the optimized GRIN-PCL operation at the designed-for frequency (50 kHz) and document broadband performance out to ± 10 kHz. Finally, a piezoelectric harvester located at the first focus of the GRIN PCL is shown to yield an increase in power output of more than 1 order of magnitude as compared with baseline energy harvesting.

ACKNOWLEDGMENTS

The authors acknowledge an anonymous reviewer for pointing out the possible effects of anisotropy on the refractive index.

[1] A. Climente, D. Torrent, and J. Sánchez-Dehesa, Gradient index lenses for flexural waves based on thickness variations, Appl. Phys. Lett. **105**, 064101 (2014).
[2] J. Zhao, R. Marchal, B. Bonello, and O. Boyko, Efficient focalization of antisymmetric Lamb waves in gradient-index phononic crystal plates, Appl. Phys. Lett. **101**, 261905 (2012).
[3] G. Milton, M. Briane, and J. Willis, On cloaking for elasticity and physical equations with a transformation invariant form, New J. Phys. **8**, 248 (2006).
[4] S. Cummer and D. Schurig, One path to acoustic cloaking, New J. Phys. **9**, 45 (2007).
[5] A. Darabi, A. Zareei, M.-R. Alam, and M. J. Leamy, Broadband bending of flexural waves: Acoustic shapes and patterns, Sci. Rep. **8**, 11219 (2018).
[6] D. Lu and Z. Liu, Hyperlenses and metalenses for far-field super-resolution imaging, Nat. Commun. **3**, 1205 (2012).
[7] C. Howells, Piezoelectric energy harvesting, Energy Convers. Manag. **50**, 1847 (2009).
[8] S. Priya and D. Inman, *Energy Harvesting Technologies* (Springer, New York, 2009), Vol. 21.
[9] S. Horowitz, M. Sheplak, L. Cattafesta III, and T. Nishida, A MEMS acoustic energy harvester, J. Micromech. Microeng. **16**, S174 (2006).
[10] L. Wu, L. Chen, and C. Liu, Acoustic energy harvesting using resonant cavity of a sonic crystal, Appl. Phys. Lett. **95**, 013506 (2009).
[11] C. Rupp, M. Dunn, and K. Maute, Switchable phononic wave filtering, guiding, harvesting, and actuating in polarization-patterned piezoelectric solids, Appl. Phys. Lett. **96**, 111902 (2010).
[12] M. Carrara, M. Cacan, M. Leamy, M. Ruzzene, and A. Erturk, Dramatic enhancement of structure-borne wave energy harvesting using an elliptical acoustic mirror, Appl. Phys. Lett. **100**, 204105 (2012).
[13] M. Carrara, M. Cacan, J. Toussaint, M. Leamy, M. Ruzzene, and A. Erturk, Metamaterial-inspired structures and concepts for elastoacoustic wave energy harvesting, Smart Mater. Struct. **22**, 065004 (2013).
[14] M. Carrara, J. Kulpe, S. Leadenham, M. Leamy, and A. Erturk, Fourier transform-based design of a patterned piezoelectric energy harvester integrated with an elastoacoustic mirror, Appl. Phys. Lett. **106**, 013907 (2015).
[15] A. Darabi and M. J. Leamy, Analysis and experimental verification of multiple scattering of acoustoelastic waves in thin plates for enhanced energy harvesting, Smart Mater. Struct. **26**, 085015 (2017).
[16] A. Darabi, M. Ruzzene, and M. J. Leamy, Piezoelectric T-matrix approach and multiple scattering of electroacoustic waves in thin plates, Smart Mater. Struct. **26**, 125018 (2017).
[17] S. Lin, T. Huang, J. Sun, and T. Wu, Gradient-index phononic crystals, Phys. Rev. B **79**, 094302 (2009).
[18] Y. Jin, D. Torrent, Y. Pennec, Y. Pan, and B. Djafari-Rouhani, Simultaneous control of the s 0 and a 0 lamb modes by graded phononic crystal plates, J. Appl. Phys. **117**, 244904 (2015).
[19] T.-T. Wu *et al.* in *Photonic and Phononic Properties of Engineered Nanostructures IV* (International Society for Optics and Photonics, 2014), Vol. 8994.
[20] H. Kurt and D. Citrin, Graded index photonic crystals, Opt. Express **15**, 1240 (2007).
[21] A. Zareei, A. Darabi, M. J. Leamy, and M.-R. Alam, Continuous profile flexural grin lens: Focusing and harvesting flexural waves, Appl. Phys. Lett. **112**, 023901 (2018).
[22] T. Wu, Y. Chen, J. Sun, S. Lin, and T. Huang, Focusing of the lowest antisymmetric lamb wave in a gradient-index phononic crystal plate, Appl. Phys. Lett. **98**, 171911 (2011).
[23] T. Wu, M. Chiou, Y. Lin, and T. Ono, Design and fabrication of a gradient-index phononic quartz plate lens, Proc. SPIE **8994**, 89940G–1 (2014).
[24] J. Zhao, B. Bonello, R. Marchal, and O. Boyko, Beam path and focusing of flexural Lamb waves within phononic crystal-based acoustic lenses, New J. Phys. **16**, 063031 (2014).
[25] S. Tol, F. Degertekin, and A. Erturk, Gradient-index phononic crystal lens-based enhancement of elastic wave energy harvesting, Appl. Phys. Lett. **109**, 063902 (2016).
[26] C. Gomez-Reino, M. Perez, and C. Bao, *Gradient-Index Optics: Fundamentals and Applications* (Springer Science & Business Media, Berlin, 2012).
[27] R. Sainidou, N. Stefanou, I. Psarobas, and A. Modinos, A layer-multiple-scattering method for phononic crystals and heterostructures of such, Comput. Phys. Commun. **166**, 197 (2005).
[28] I. Psarobas, N. Stefanou, and A. Modinos, Scattering of elastic waves by periodic arrays of spherical bodies, Phys. Rev. B **62**, 278 (2000).
[29] L. Cai and S. Hambric, Multiple scattering of flexural waves on thin plates, J. Vib. Acoust. **138**, 011009 (2016).
[30] A. Sharma, D. Kumar, and A. Ghatak, Tracing rays through graded-index media: A new method, Appl. Opt. **21**, 984 (1982).